American Journal of Mechanical Engineering, 2020, Vol. 8, No. 1, 40-49
Available online at http://pubs.sciepub.com/ajme/8/1/5
Published by Science and Education Publishing
DOI:10.12691/ajme-8-1-5

A Computational Fluid Dynamics Investigation of a Numerically Simulated Wave Tank

Mohammad Nasim Uddin[1], Michael Atkinson[2,*], Frimpong Opoku[3]

Department of Mechanical Engineering, North Carolina A&T State University, Greensboro, NC, USA
*Corresponding author: mdatkinson@ncat.edu

Received April 20, 2020; Revised May 22, 2020; Accepted May 29, 2020

Abstract In this paper, a two-dimensional Numerical Wave Tank (NWT) is proposed to calculate the static pressure variation along the lower wall of an experimental wave-flume. The experimental setup was a 4.72m long wave flume with a flap-type wave-maker. The experiments were carried out at various water heights of 100mm, 80mm, and 60mm, with a motor speed of 60 rpm. The numerical simulations were completed using ANSYS™ Fluent, with two sets solutions: 1) the unsteady, three-dimensional Reynolds Averaged Navier-Stokes (URANS) equations coupled with a k-ε turbulence model; 2) unsteady 3-D Euler equations. In both computations, the volume of fluid (VOF) method was used to capture the free surface and a grid independence study was completed. The unsteady Euler simulations showed the best agreement to the experimental results. Several cases were run to complete validation and verification of the numerical model, and the CFD results are in good agreement with the experiment. Thus, for small two-dimensional experimental wave flumes, the unsteady inviscid, volume of fluid method can accurately predict surface pressure distribution.

Keywords: *numerical wave tank, flap-type wavemaker, volume of fluid, Reynolds averaged Navier Stokes*

Cite This Article: Mohammad Nasim Uddin, Michael Atkinson, and Frimpong Opoku, "A Computational Fluid Dynamics Investigation of a Numerically Simulated Wave Tank." *American Journal of Mechanical Engineering*, vol. 8, no. 1 (2020): 40-49. doi: 10.12691/ajme-8-1-5.

1. Introduction

Ocean renewable energy is an attractive eco-friendly alternative to fossil fuels. Population growth coupled with increasing energy demands, motivates the need to explore and extract previously untapped forms of energy. Renewed interest in ocean wave energy extraction has led to the improvement and deployment of large-scale wave energy extraction devices. Current research reveals that Earth's oceans contain a large amount of energy, 30,000 TWh/year, and can fulfill global electricity demands if it is harnessed efficiently. However, the uncertainty of ocean wave, current prediction, natural disasters, and inefficient designs make ocean energy extraction challenging.

For many years, successful high-quality experiments using laboratory-produced ocean waves have been carried out. Two of the most commonly used laboratory techniques, for the study of the interaction between water waves and marine structures, are wave flumes (two-dimensional) and wave tanks (three dimensional). In most cases, either piston- or flap-type wavemakers are used in wave tanks. The piston-type wavemaker is suitable to generate shallow water waves whereas, in deep water, the flap-type is more efficient. [1] However, numerous challenges exist, such as cost, equipment "down-time", large scale facility size, and long run-times are necessary to generate quality data. An alternative approach to experimental methods is to numerically model wave flumes or tanks, which can be successfully used to model wave energy converters. [2] Currently, researchers are exploring the ability of numerical wave tanks to predict the efficiency of marine energy extraction devices. In literature, two main approaches to numerically simulate wave flumes are reported: 1) numerical models assuming inviscid and irrotational flow, and 2) numerical models considering the fluid's viscosity [3]. Some complications, such as moving boundaries at the free surface, wavemaker boundary conditions, and the selection of suitable far-field non-reflecting boundary conditions are critical for accurate simulations of numerical wave tanks.

For the treatment of free-surface flows, only three types of computational methods exist to date: 1) Interface tracking method [4] / interface capturing method (modified marker-and-cell [5], 2) volume of fluid [6]) and, 3) a hybrid method [7].

When the fluid flow is irrotational and inviscid, the Boundary Element Method (BEM) is an efficient and economic choice for water wave simulation. [8] However, these numerical models produce unwanted reflected waves from structures with an open boundary and should be minimized for accurate results. As a result, absorption boundary conditions [9,10], and radiation boundary conditions [11,12] are implemented to reduce wave reflection impact. [13] Israeli et al. [14] developed a survey of methods for implementing radiation boundary

conditions to offer improvements over the other methods. Boo and Kim et al. [15] developed a nonlinear numerical wave tank using a three-dimensional higher-order boundary element method (HOBEM) and made comparisons between linear and nonlinear waves generated numerically with theoretical input waves. The BEM technique has difficulty treating the open boundary condition to have a non-reflecting NWT, they implemented the Orlanski radiation condition at the downstream tank boundary and concluded that it is valid and effective even for steep irregular waves. However, the radiation boundary condition still assumes the constant phase velocity which makes the model invalid for irregular wave field. Ohyama and Nadaoka et al [16] suggested a two-dimensional numerical wave tank using a BEM-based absorption numerical filter for the treatment of open boundary conditions which makes it capable of analyzing both regular and irregular wave fields.

In the recent years, the increase of computational power enables researchers to explore the development of nonlinear NWTs. As a result, fully 3-D numerical wave tanks have also been studied [17,18].

The introduction of a mass source function [19] to the continuity equation [20,21,22], and an additional forcing function in the momentum equation [23,24] can produce a variety of three-dimensional waves.

Direct Numerical Simulation (DNS) is effective when the Reynolds number of the fluid is minimal, and the computational domain is small [25]. As an alternative to DNS, Reynolds Averaged Navier-Stokes (RANS) equations [26,27] and Large Eddy Simulation (LES) [28] can greatly reduce the computational load compared to that of DNS. Elhanafi et al. [29] used ANSYS FLUENT™ based RANS equations and Volume of Fluid (VOF) method to investigate ocean wave energy generation. Liu et al. [30] presented an NWT implemented with ANSYS FLUENT™ using a two-phase VOF model for incompressible viscous flow to investigate the performance of the Oscillating Water Column (OWC) wave energy converter.

Zabihi et al. [31] used two separate software packages, namely FLUENT™ and Flow-3D to create regular gravity waves in a numerical wave tank. They compared free surface elevation and x-velocity of wave-particle from both of the above mentioned CFD tools with the theoretical results. They found that Flow-3D results provide higher accuracy in calculating free surface elevation.

Nonlinear free-surface simulations are still computationally expensive, so 2-D NWTs [32] have been developed. Dong and Huang et al. [33] developed a 2-D numerical wave tank to simulate different incident waves of small- and finite- amplitude and solitary waves. Park et al. investigated characteristics of non-linear wave motions and their interactions with a stationary 3-D body inside an NWT implementing a finite-difference/volume method based on the Navier-Stokes (NS) equations and a modified marker-and-cell (MAC) method for the treatment of the free surface.

The simulations carried out in this study solved the unsteady 3-D RANS equations coupled to the realizable k-ε turbulence closure model and are solved in conjunction with the volume of fluid method using FLUENT™. Here, pressure-velocity coupling was completed using the Pressure-Implicit with Splitting of Operators (PISO) algorithm and dynamic meshing [34,35] was used to simulate a moving wall at the inlet boundary representative of the flap-type wavemaker. By implementing a user-defined function [36] as an input to FLUENT™, dynamically structured meshing was completed. To prevent wave reflection, a damper with a mild slope was used on the opposite end of the flume. The static pressure is plotted versus time and a comparison of the numerical and experimental results is presented. A Grid independence study [37,38] was performed to validate the numerical model.

2. Materials and Methods

For the simulations carried out in this investigation, we modeled a flap-type wavemaker using ANSYS FLUENT™. This wavemaker has no translational velocity, but can be modeled as a simple harmonic angular velocity and is defined as follows: [39]

$$\theta(t) = \frac{\Delta\theta}{2}\cos\frac{2\pi}{T}t \tag{1}$$

Where Δθ represents the angular span of the wavemaker. Since the stroke length of the flap-type wavemaker is related to both the angular span and still water depth by the following equation,

$$S = 2dtan\frac{\Delta\theta}{2}. \tag{2}$$

Solving for Δθ,

$$\Delta\theta = 2\tan^{-1}\left[\frac{S}{2d}\right]. \tag{3}$$

Hence, we get the original equation as,

$$\theta(t) = \tan^{-1}\left[\frac{S}{2d}\right]\cos\left[\frac{2\pi t}{T}\right]. \tag{4}$$

Differentiating with respect to t, we get,

$$\frac{d\theta}{dt} = -(2\pi)\left[\tan^{-1}\left[\frac{S}{2d}\right]\sin\left[\frac{2\pi t}{T}\right]\right]. \tag{5}$$

But the linear velocity is connected to the angular velocity by the following expression,

$$v = \omega r \tag{6}$$

$$v = r\frac{d\theta}{dt} \tag{7}$$

$$v = -(2\pi r)\left[tan^{-1}\left[\frac{S}{2d}\right]\sin\left[\frac{2\pi t}{T}\right]\right]. \tag{8}$$

The wave period can be obtained by the equation,

$$T = \frac{t}{N}. \tag{9}$$

2.1. Numerical Solutions

The matrix shown in Table 1 was developed to help guide the NWT simulations for comparison to the experimental data. For the simulations, at first, two uniform meshes were generated: a coarse mesh and a fine mesh with cell sizes of 5mm and 10mm, respectively. For each grid size, three separate water heights with a motor speed of 60 rpm were used.

Table 1. Matrix 1 of Numerical Simulation

Water Height d(mm)	Motor Speed (rpm)	Mesh		Model	
100	60	coarse	fine	turbulent	inviscid
80					
60					

Our numerical simulations using the realizable k-ε RANS turbulence model did not show good agreement to the experimental data. However; the unsteady, inviscid Euler equations exhibited better agreement and accurately captured the trends of the experimental data. Hence, only the inviscid model was used for the later simulations, as directed in Table 2. To complete a grid independence study Cartesian meshes of four different grid sizes: coarse (4cm), medium (2cm), fine (1cm) and extra fine (4mm) were used. As a result, 24 distinct simulations were completed.

Table 2. Matrix 2 of Numerical Simulation

Water Height d(mm)	Motor Speed (rpm)	Mesh				Model
100	60	coarse	medium	fine	extra fine	inviscid
80						
60						

2.1.1. Experimental Setup

The experimental setup is shown in Figure 1. The wave tank dimensions are: Length: 4.72m, Width: 0.065m, Depth: 0.24m. A flap-type wave maker is employed at one end to produce desired waves in the wave tank. A mild slope is attached to the other end of the wave tank to dampen out the effects of the reflecting waves.

Experiments were carried out for 3-different water heights (100mm, 80mm, 60mm) with a constant motor speed of 60 rpm. To measure the static pressure variation along the bottom surface of the wave tank, pressure sensors were placed at 5 different locations, P_1-P_5.

Our in-house wave tank was purchased as a finished product with default positions for the sensors [Table 3]. For the simulations and experiments performed in this study, we used the prescribed pressure locations for comparisons.

To better characterize the wave-flume, future studies will explore the use of supplementary instrumentation including additional pressure sensors, a flow meter, a high-fidelity camera, and a piston-type wavemaker.

Table 3. Sensors Locations

	Sensors				
	P_1	P_2	P_3	P_4	P_5
Location	0.559m	1.392m	2.225m	3.058m	3.891m

Table 4. Experimental Waves specifications

Water Height d (mm)	Wave Height (mm)	Wave Period (s)	Motor Speed (rpm)
100	24.02	1.07	60
80	18.72	1.03	
60	15.18	0.979	

Each sensor was set to record the pressure data in mm of water for approximately 40 seconds. Figure 5 shows the pressure variation over time for the various pressure sensors at an rpm of 60, of wave height of 100mm.

Wave periods and wave heights were extracted using 'LabVIEW' data acquisition system as shown in Figure 4.

2.1.2. Equations

Applying the Eulerian approach of mass, momentum, and energy, the governing equations used in the simulations were the incompressible, three-dimensional Navier-Stokes equations shown below:

$$\nabla.\vec{U} = 0 \tag{10}$$

The velocity field of an incompressible flow is divergence-free for the fluid. Here, $\vec{U}$ denotes the velocity of the fluid. The momentum equation (the Navier-stokes equation) is as following:

$$\rho\left(\frac{\partial\vec{U}}{\partial t}+\left(\vec{U}.\nabla\right)\vec{U}\right)=-\nabla p+\mu\nabla^2\vec{U}+\vec{F} \tag{11}$$

Where p and ρ denote pressure and density, respectively. The terms μ and $\vec{F}$ are the viscosity and the external body force acting per unit mass (i.e. drag force) of the fluid, respectively. The Euler equation applied to inviscid flow is given by:

$$\rho\frac{D\mathbf{V}}{Dt}=\rho\mathbf{g}-\nabla p. \tag{12}$$

Turbulence models used to close the set of the RANS equations, are commonly used to account for the effects of turbulence with reasonable computational cost and accuracy. [40] The $k-\omega$ turbulence model has good accuracy in near wall region but poor predictions in the far field. Large Eddy Simulations (LES) are computationally costly but are highly accurate at capturing turbulent effects up to a particular length scale.

The standard $k-\epsilon$ model is computationally cheap and has good accuracy in far wall regions, though the predictions for the near-wall regions are poor. The Realizable $k-\epsilon$ model is straightforward, robust, and has a physical model for the ϵ transport equation and the eddy viscosity.

Realizable $k-\epsilon$ model was adopted to calculate the results of turbulence phenomena, as shown in the following equations, [41]

$$\frac{D}{Dt}(\rho k)=\frac{\partial}{\partial y}\left[\left(\mu+\frac{\mu_t}{\sigma_k}\right)\frac{\partial k}{\partial y}\right]+\mu_T\left(\frac{\partial u}{\partial y}\right)^2$$

$$-\rho\epsilon-2\mu\left(\frac{\partial k^{\frac{1}{2}}}{\partial y}\right)^2$$

$$\frac{D}{Dt}(\rho\epsilon)=\frac{\partial}{\partial y}\left[\left(\mu+\frac{\mu_t}{\sigma_\epsilon}\right)\frac{\partial\epsilon}{\partial y}\right]+c_1 f_1\frac{\epsilon}{k}\mu_T\left(\frac{\partial u}{\partial y}\right)^2 - c_2 f_2\frac{\rho\epsilon^2}{k}+2\mu\mu_T\left(\frac{\partial^2 u}{\partial y^2}\right) \quad (13)$$

Where Turbulent viscosity is calculated by the following formula:

$$\mu_t=\rho C_\mu f_\mu\frac{k^2}{\epsilon}. \quad (14)$$

And turbulent thermal conductivity is found by the following equation:

$$k_T=c_p\mu_T/0.9. \quad (15)$$

The influence of Reynolds number is introduced by way of the f's as following:

$$f_1=1,\ f_2=1-0.3\exp\left(-R^2\right)$$

$$f_\mu=\exp\left[-\frac{2.5}{\left(1+\frac{R}{50}\right)}\right]. \quad (16)$$

Where $R=\frac{\rho k^2}{\mu\epsilon}$ may represent the Reynolds number of turbulences. Values of the empirical constants are as follows: $c_\mu=0.09,\ c_1=1.55,\ c_2=2.0,\ \sigma_k=1.0\ \ \sigma_\epsilon=1.3.$

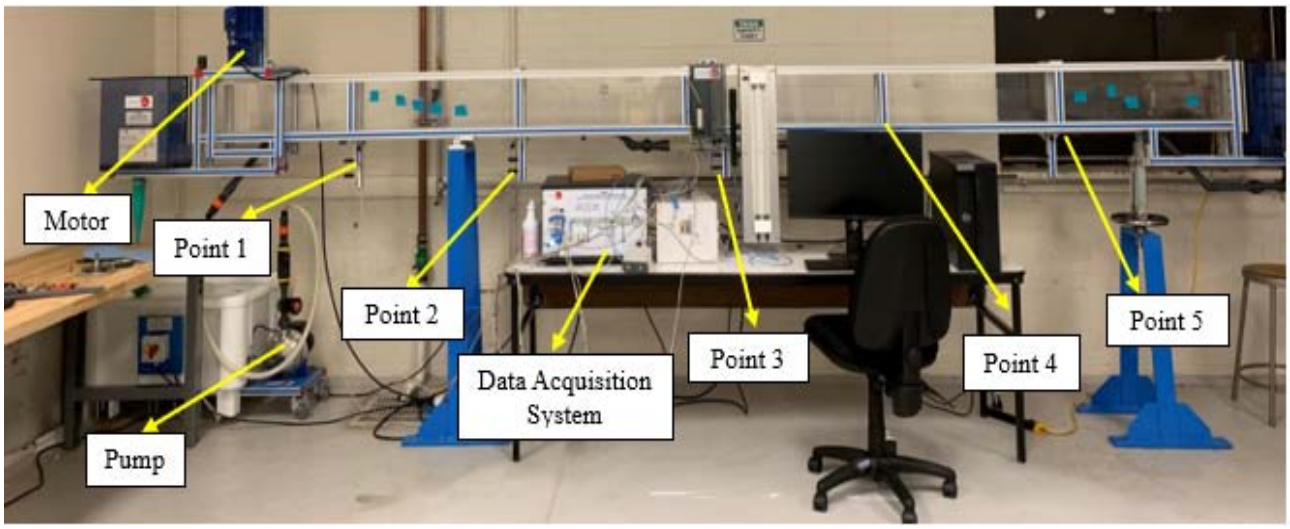

Figure 1. Experimental wave flume

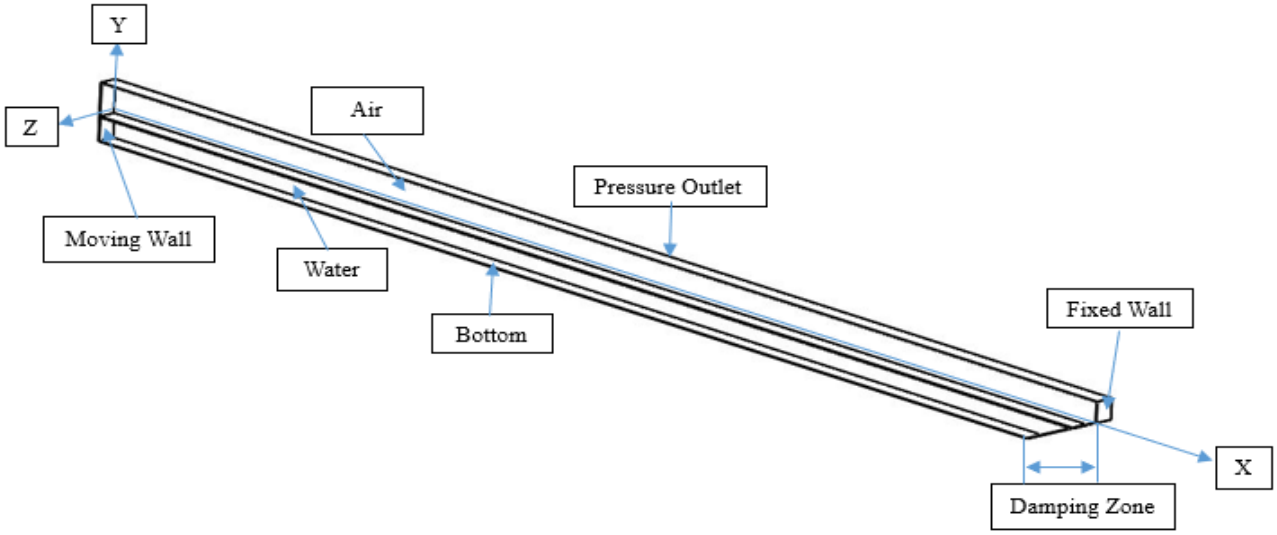

Figure 2. Numerical wave tank model

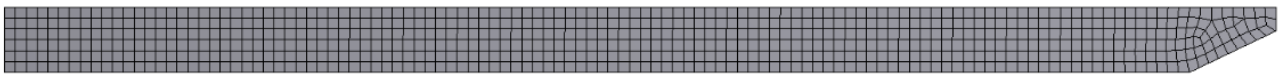

Figure 3. Computational mesh generated in Ansys Fluent.

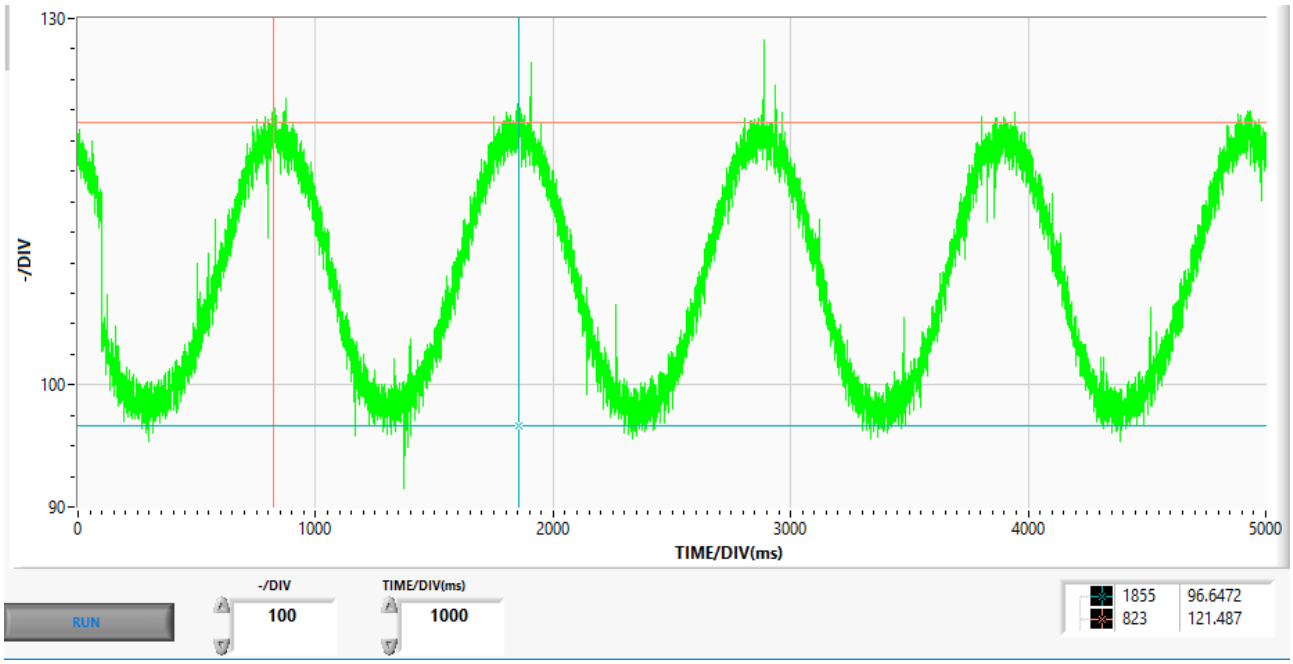

Figure 4. Wave characteristics in oscilloscope

The VOF method, introduced by Hirt et al. [42], was used to simulate multiphase flow. In this method, the fluid volume fraction is calculated in each cell while all fluids share a single set of momentum equations. To distinguish between different fluids using a volume fraction, a scalar quantity ϕ is used and is defined by,

$$\phi = \begin{cases} 0 \\ 0 < \phi < 1 \\ 1 \end{cases} \begin{matrix} liquid \\ gas \sin terface \\ liquid \end{matrix}. \quad (17)$$

The continuity equation of the volume fraction is solved to keep track of the air-water interface. For the m'th fluid in a system of n fluids, the continuity equation is given by:

$$\frac{\partial \phi_m}{\partial t} + \vec{U}.\nabla \phi_m = 0 \quad (18)$$

$$\sum_{m=1}^{n} \phi_m = 1. \quad (19)$$

2.1.3. Numerical Models

To mimic the experimental wave-flume, a 2-D NWT with the same dimensions was constructed: Length: 4.72m, Width: 0.065m, Depth: 0.24m. Two phases of fluid are considered: air (primary) and water (secondary), and are assumed to be incompressible, inviscid, irrotational, and immiscible.

The boundary conditions implemented on the computational domain of the numerical wave tank are as follows. The bottom and right walls: a no-slip wall boundary condition was imposed. The left wall boundary condition was set to a moving wall, to account for the motion of the wavemaker, a time-dependent velocity equation was developed and specified by a User Defined Function (UDF). The top wall boundary was set to the atmospheric pressure. A symmetry boundary condition was applied at both the front and the back walls. In Table 5, all the implemented boundary conditions are shown.

Table 5. Boundary Conditions

Boundary	Boundary Conditions Type
Bottom	Wall
Right	Wall
Top	Pressure outlet
Left	Wall
Front	Symmetry
back	Symmetry

A flap-type wave maker generated regular waves following the time-dependent velocity equation at the left boundary through the wave generation domain. For the treatment of reflection of waves back into the computational domain, a mild slope, was constructed, was represented as the damping zone in Figure 2.

The initial numerical simulations used a k-ε turbulence model with a UDF for a time-dependent velocity equation for the wavemaker. Figure 3 shows the coarse mesh that was used for the simulations. The statistics of the meshes are shown in Table 6.

Table 6. Grid Sizes

Mesh	Cell Size (mm)	No. of Cells
coarse	10	57000
fine	5	372400

Figure 6-8 show contours of pressure, volume fraction, and velocity from the RANS solutions. Figure 9-13 show a comparison of the experimental vs. computational pressure values. The results show a significant discrepancy between the numerical and experimental results. This is due to the strong reflection of the waves off of the inclined damper. This is evident in the strong oscillations in the numerical pressure data. The experimental setup did not have this reflection.

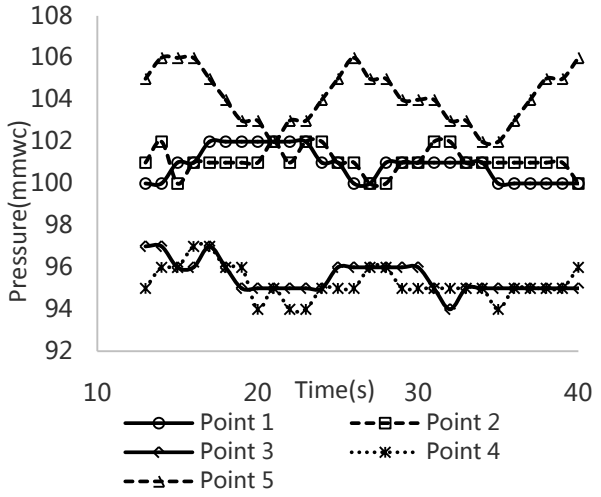

Figure 5. Pressures at different sensor locations for 100 mm water height

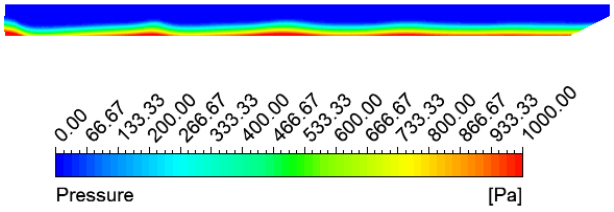

Figure 6. Pressure Contours

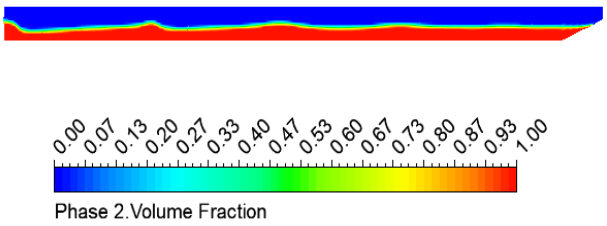

Figure 7. Volume fraction contours.

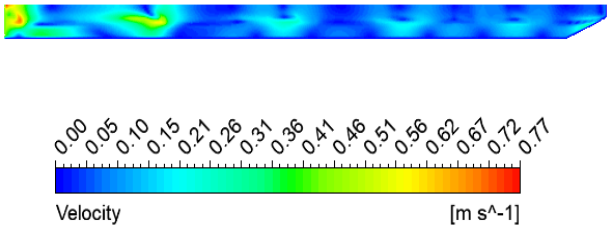

Figure 8. Velocity contours

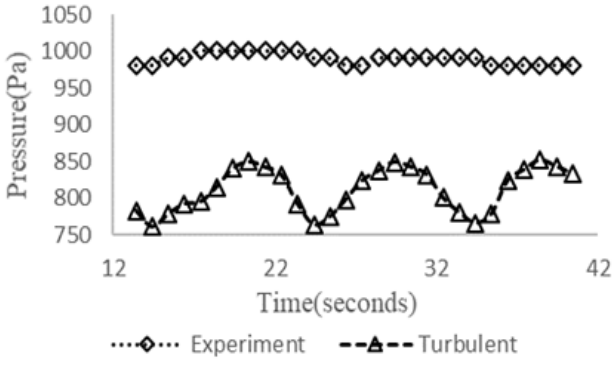

Figure 9. Comparison of experimental vs numerical pressure at point 1

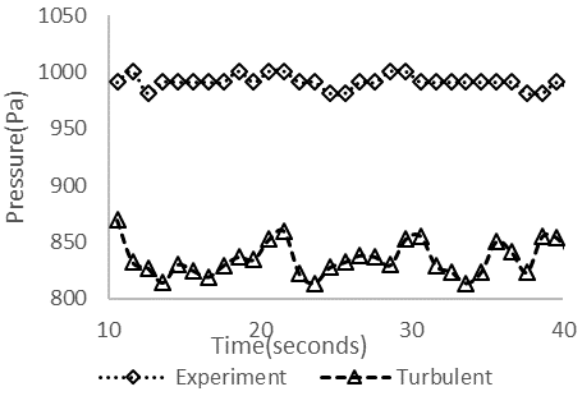

Figure 10. Comparison of experimental vs numerical pressure at point 2

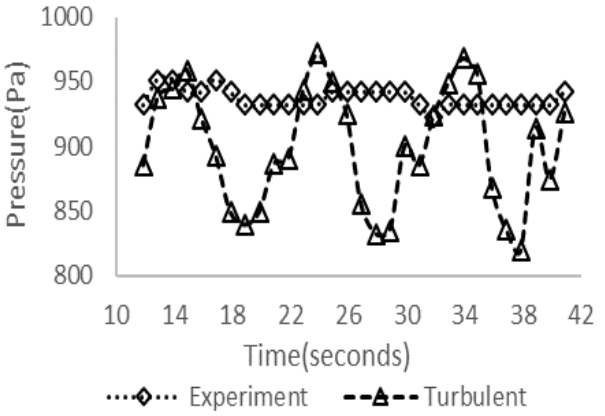

Figure 11. Comparison of experimental vs numerical pressure at point 3

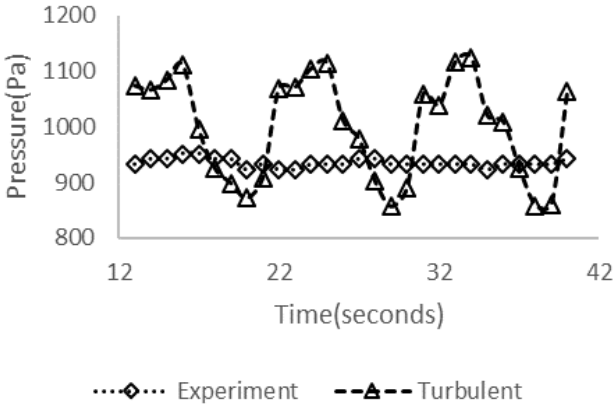

Figure 12. Comparison of experimental vs numerical pressure at point 4

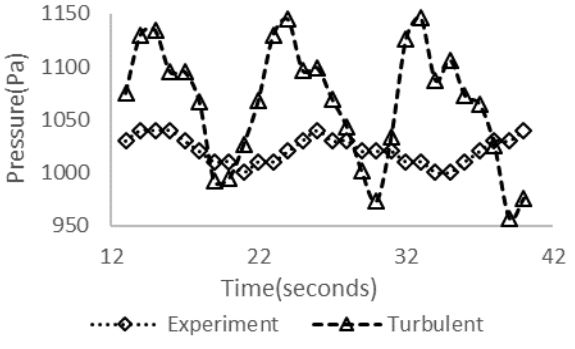

Figure 13. Comparison of experimental vs numerical pressure at point 5

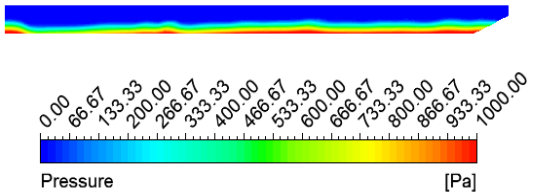

Figure 14. Pressure contours

Figure 9-13 show that the experimental data has a large discrepancy compared to the numerical results using the realizable k-ε turbulent model. In an effort to test a simple NWT model, we computed inviscid solutions to compare to the experiment. An inviscid model was implemented in FLUENT™ and contours of pressure, volume fraction, and velocity, are shown in Figure 14-16, extracted at 71 seconds.

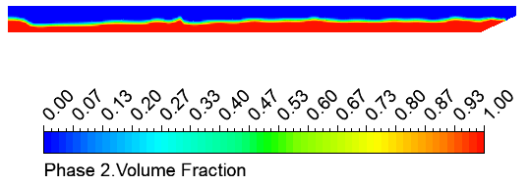

Figure 15. Volume fraction contours.

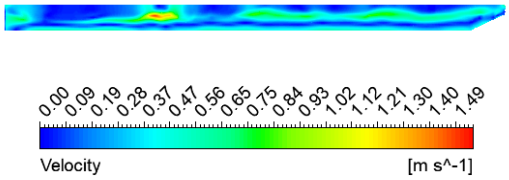

Figure 16. Velocity contours

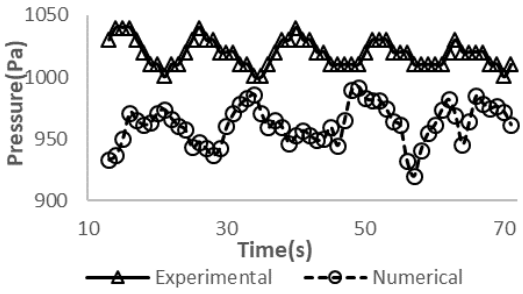

Figure 17. Comparison of experimental vs numerical pressure at point 5 for 100 mm water height

From Figure 17, we determined that there is better agreement between the experimental and numerical data for 100 mm water height, at 71 seconds.

In Figure 18, the numerical simulations showed better agreement and captured the trends of the experimental data. The inviscid results also showed better agreement with the computed wavelength and absolute values than the RANS simulations, however, the results were out of phase. Thus, verifying that oscillations due to wave reflection were somewhat damped out but not completely eliminated.

Furthermore, to achieve consistent results, a Cartesian gridding method was introduced to generate a uniform structured mesh. To show a grid independent solution, 4 different mesh sizes were used and categorized as coarse, medium, fine, and extra fine; depending on the number of cells. The actual numbers of the cells in the meshes generated throughout the computational domain are shown in Table 7.

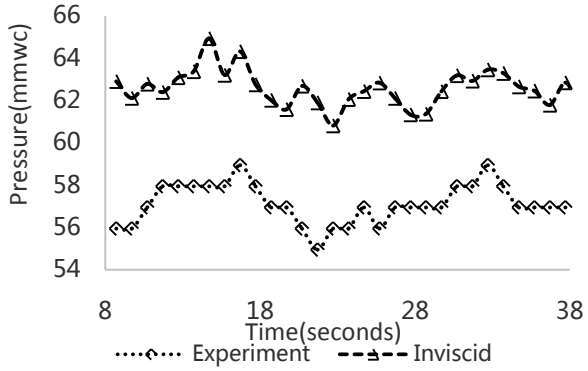

Figure 18. Comparison of experimental vs numerical pressure at point 5 for 60 mm water height

Table 7. Cartesian Grid Sizes

Mesh	Cell size (cm)	No. of Cells
Coarse	4.0	870
Medium	2.0	9696
Fine	1.0	94017
Extra fine	0.4	1293336

The simulations were carried out using a dual octo-core Intel Xeon processor workstation with 32GB RAM and a processor speed of 3.4Ghz. The convergence criterion was 1E-04 for the continuity equation and 1E-06 for the momentum equations for inner-iterations. An average of 100 inner iterations was needed for convergence.

Table 8. Modelling in Ansys Fluent R19.1

Analysis	Unsteady
Multiphase model	Volume of Fluid (VOF)
Fluid	Air and Water (liquid)
Viscosity	Inviscid
Dynamic mesh	Layering method
Pressure-velocity coupling	PISO
Momentum discretization	Second-order upwind
Under relaxation factors	Default
Initialization	Hybrid
Time steps size	0.0005

2.1.4. Validation of Numerical Wave Tank

Like the experimental waves, the numerical waves were generated throughout the wave tank with the same wave period and wavelength. Wave propagation in the numerical wave tank is shown in Figure 19 - Figure 25.

Figure 19. Wave propagation at t=0s

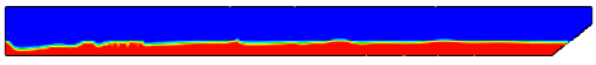

Figure 20. Wave propagation at t=5s

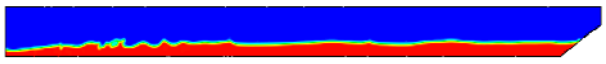

Figure 21. Wave propagation at t=10s

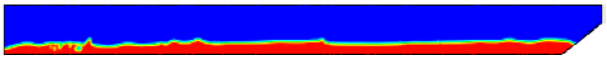

Figure 22. Wave propagation at t=15s

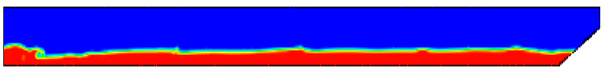

Figure 23. Wave propagation at t=20s

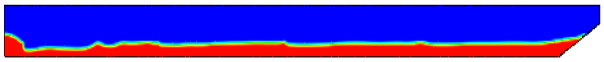

Figure 24. Wave propagation at t=25s

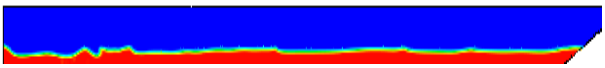

Figure 25. Wave propagation at t=29.94s

From the above figures, it is shown that the wave propagates from the left to the right which complements the udf driven left boundary condition of the numerical wave tank. The volume fraction of both of the fluids are, changing over time, apparently clear by two distinct colors: blue and red, which corresponds to air and water, respectively. Reflection of waves back into the computational domain was somewhat lessened by the mild slope.

The numerical results obtained after incorporating the aforementioned meshes and tools as dictated by Table 7 and Table 8. To verify the numerical modeling, numerical and experimental data were compared at a time sufficient enough to stabilize the wave pattern in the wave tank. Numerical probes were placed at 5 distinct positions on the wave tank to replicate the pressure sensors in the experimental setup.

The grid independence study conducted is shown in Figure 26-30. The numerical and experimental static pressure distribution at the designated sensor locations were compared after the wave achieved steady propagation along the wave tank (9.4 s in this case). The computational results of the coarse and medium grids somewhat followed the experimental data trends but tended to show large discrepancies compared to the experimental data. Figure 28 shows that there is a large deviation at point 3 for all of the numerical results. It is most likely the result of erroneous data recorded by the pressure sensor at that particular point. The sensor wires were adjusted because of an inadequacy of the space required to fit them properly in place. Therefore, the results might be affected and eventually accounts for the discrepancy found between the experimental and numerical data.

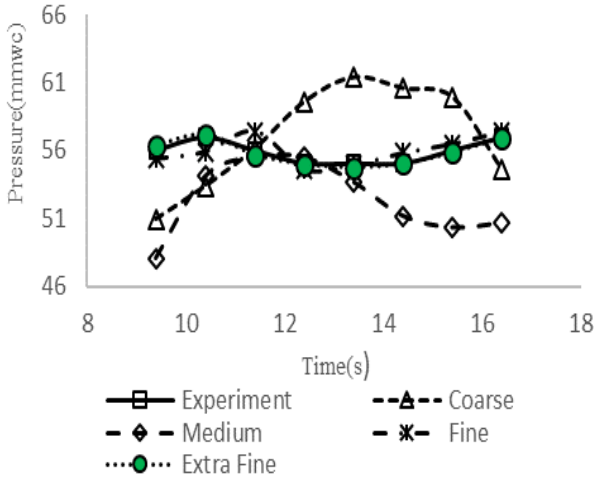

Figure 26. Grid independence at point 1 for 60 mm water height

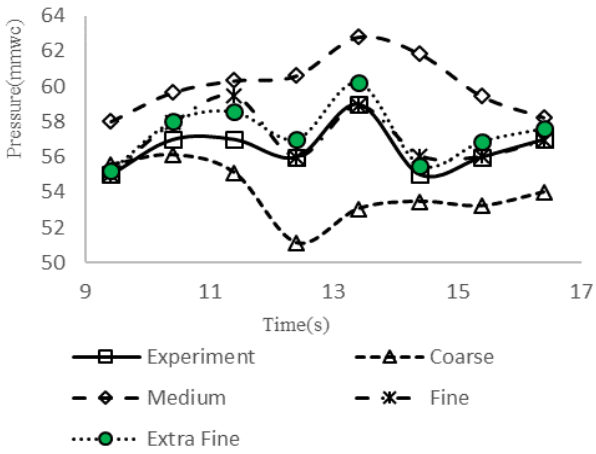

Figure 27. Grid independence at point 2 for 60 mm water height

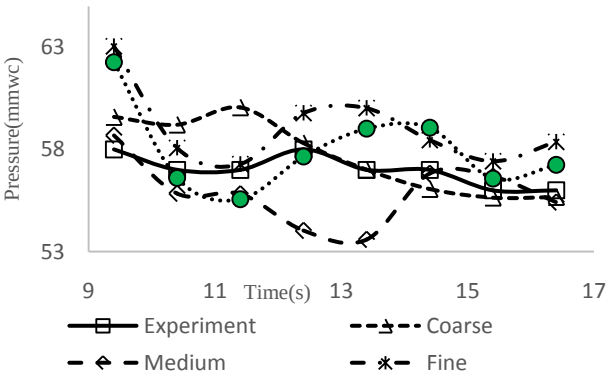

Figure 28. Grid independence at point 3 for 60 mm water height

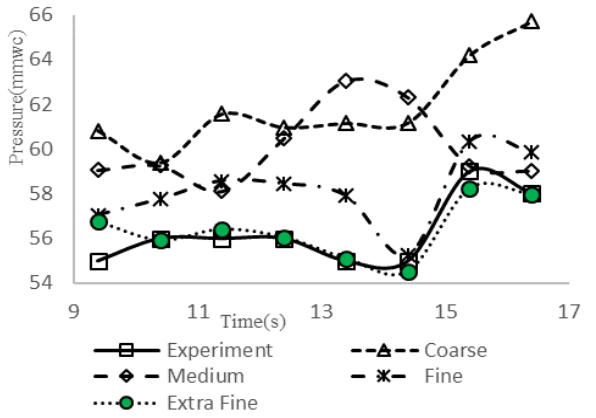

Figure 29. Grid independence at point 4 for 60 mm water height

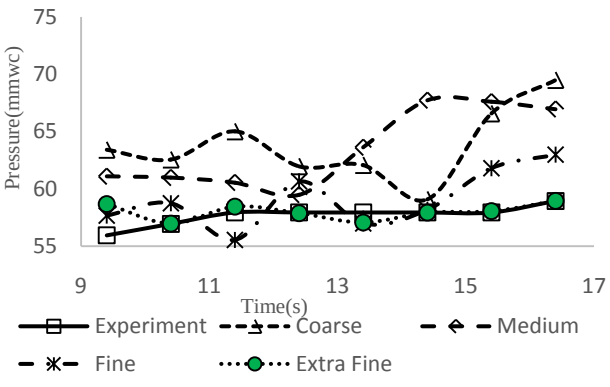

Figure 30. Grid independence at point 5 for 60 mm water height

However, upon the introduction of the fine meshes, except for point 3, the discrepancy was mitigated to a tolerable limit. And finally, with the increase of more grid points (extra fine grids) in the computational domain, numerical modeling of the wave-flume is validated.

3. Conclusion

The validation of a two-dimensional numerical wave flume is presented in this paper. Verification was provided for several cases. The simulations were carried out using the three-dimensional unsteady Euler and the Reynolds Averaged Navier-Stokes equations. Comparison of the surface pressure showed that the Euler solutions had better agreement with the experimental results. Based on this, the three-dimensional RANS simulations are not required to achieve accurate predictions for small-scale wave flumes, thus substantially decreasing the numerical cost. The results show that significant wave reflection causes large-scale oscillating pressure fluctuations, which valuated the need to use "non-reflecting wave" boundary conditions, to produce more accurate results.

Acknowledgements

This research was partially supported by [North Carolina Renewable Ocean Energy Program].

Nomenclature

d	still water depth, m
$\vec{F}$	external body force acting per unit mass, $\frac{N}{kg}$
g	gravitational acceleration, $\frac{m}{s^2}$
k	turbulent kinetic energy per unit mass, $\frac{m^2}{s^2}$
N	number of revolutions, rpm
p	pressure, Pa
r	radius of the flap, m
S	stroke length, m
t	time, s
T	wave period, s
$\vec{U}$	velocity, $\frac{m}{s}$
v	linear velocity, $\frac{m}{s}$
ω	angular velocity, $\frac{rad}{s}$
ρ	density, $\frac{kg}{m^3}$
μ	viscosity, Pa.s
ϵ	turbulent kinetic energy dissipation rate, $\frac{m^2}{s^3}$
μ_t	eddy viscosity, $\frac{m^2}{s}$
Δθ	angular span of the wavemaker, rad
θ	angular displacement, rad

References

[1] R. G. Dean and R. A. Dalrymple, Water wave mechanics for engineers and scientists. 1984.

[2] M. Horko, "CFD Optimisation of an Oscillating Water Column Wave Energy Converter," M.Sc Thesis. Univ. West. Aust., pp. 1-159, 2007.

[3] S. T. Grilli and J. Horrillo, "Numerical generation and absorption of fully nonlinear periodic waves," J. Eng. Mech., vol. 123, no. 10, pp. 1060-1069, 1997.

[4] D. B. Kothe, M. W. Williams, K. L. Lam, D. R. Korzekwa, P. K. Tubesing, and E. G. Puckett, "A second-order accurate, linearity-preserving volume tracking algorithm for free surface flows on 3-D unstructured meshes," Proc. 1999 3rd ASME/JSME Jt. Fluids Eng. Conf. FEDSM'99, San Fr. California, USA, 18-23 July 1999, p. 1, 1999.

[5] J. C. Park, M. H. Kim, H. Miyata, and H. H. Chun, "Fully nonlinear numerical wave tank (NWT) simulations and wave run-up prediction around 3-D structures," Ocean Eng., vol. 30, no. 15, pp. 1969-1996, 2003.

[6] V. R. Gopala and B. G. M. van Wachem, "Volume of fluid methods for immiscible-fluid and free-surface flows," Chem. Eng. J., vol. 141, no. 1-3, pp. 204-221, 2008.

[7] J. Maljaars, R. J. Labeur, M. Möller, and W. Uijttewaal, "A Numerical Wave Tank Using a Hybrid Particle-mesh Approach," Procedia Eng., vol. 175, pp. 21-28, 2017.

[8] Z. Sun, Y. Pang, and H. Li, "Two dimensional fully nonlinear numerical wave tank based on the BEM," J. Mar. Sci. Appl., vol. 11, no. 4, pp. 437-446, 2012.

[9] B. Engquist and A. Majdat, "Absorbing Boundary," Encycl. Comput. Neurosci., vol. 74, no. 5, pp. 125-125, 2015.

[10] Y. Gao, H. Song, J. Zhang, and Z. Yao, "Comparison of artificial absorbing boundaries for acoustic wave equation modelling," Explor. Geophys., vol. 48, no. 1, pp. 76-93, 2017.

[11] S. F. Baudic, A. N. Williams, and A. Kareem, "A two dimensional numerical wave flume - Part 1: Nonlinear wave generation, propagation, and absorption," J. Offshore Mech. Arct. Eng., vol. 123, no. 2, pp. 70-75, 2001.

[12] R. L. Higdon, "Radiation boundary conditions for elastic wave propagation," SIAM J. Numer. Anal., vol. 27, no. 4, pp. 831-869, 1990.

[13] Y. L. Chen and S. C. Hsiao, "Generation of 3D water waves using mass source wavemaker applied to Navier-Stokes model," Coast. Eng., vol. 109, pp. 76-95, 2016.

[14] M. Israeli and S. A. Orszag, "Approximation of radiation boundary conditions," J. Comput. Phys., vol. 41, no. 1, pp. 115-135, 1981.

[15] S. Boo, "A Numerical Wave Tank For Nonlinear Irregular Waves By 3-D Higher Order Boundary Element Method," no. August, 2016.

[16] T. Ohyama and K. Nadaoka, "Development of a numerical wave tank for analysis of nonlinear and irregular wave field," Fluid Dyn. Res., vol. 8, no. 5-6, pp. 231-251, 1991.

[17] S. Y. Boo and K. N. Academy, "f f," vol. 111, 1996.

[18] S. T. Grilli, S. Vogelmann, and P. Watts, "Development of a 3D numerical wave tank for modeling tsunami generation by underwater landslides," Eng. Anal. Bound. Elem., vol. 26, no. 4, pp. 301-313, 2002.

[19] Z. Ma, T. Zhou, J. Sun, and G. Zhai, "Simulation on tsunami-like solitary wave run-up around a conical island using a modified mass source method," Eng. Appl. Comput. Fluid Mech., vol. 13, no. 1, pp. 849-859, 2019.

[20] J. S. Zhang, Y. Zhang, D. S. Jeng, P. L. F. Liu, and C. Zhang, "Numerical simulation of wave-current interaction using a RANS solver," Ocean Eng., vol. 75, pp. 157-164, 2014.

[21] J. L. Lara, N. Garcia, and I. J. Losada, "RANS modelling applied to random wave interaction with submerged permeable structures," Coast. Eng., vol. 53, no. 5-6, pp. 395-417, 2006.

[22] H. L. Wu, S. C. Hsiao, W. Y. Hsu, R. Y. Yang, and H. H. Hwung, "Dynamic response of density-stratified fluid in a submarine rectangular trench," J. Hydro-Environment Res., vol. 9, no. 1, pp. 61-80, 2015.

[23] K. Iwata, K. Kawasaki, and D. S. Kim, "Breaking limit, breaking and post-breaking wave deformation due to submerged structures," Proc. Coast. Eng. Conf., vol. 2, pp. 2338-2351, 1997.

[24] X. Feng and W. Wu, "Generation of Water Waves Using Momentum Source Wave-Maker Applied to a RANS Solver," Math. Probl. Eng., vol. 2019.

[25] J. C. Park, M. H. Kim, and H. Miyata, "Fully non-linear free-surface simulations by a 3D viscous numerical wave tank," Int. J. Numer. Methods Fluids, vol. 29, no. 6, pp. 685-703, 1999.

[26] J. Bai, N. Ma, and X. Gu, "Numerical Simulation of Focused Wave and Its Uncertainty Analysis," J. Shanghai Jiaotong Univ., vol. 23, no. 4, pp. 475-481, 2018.

[27] X. Hu, Y. Jiang, and D. Cai, "Numerical Modeling and Simulation of Wave Impact of a Circular Cylinder during the Submergence Process," Model. Simul. Eng., vol. 2017, 2017.

[28] C. Jiang, X. Liu, Y. Yao, and B. Deng, "Numerical investigation of solitary wave interaction with a row of vertical slotted piles on a sloping beach," Int. J. Nav. Archit. Ocean Eng., vol. 11, no. 1, pp. 530-541, 2019.

[29] A. Elhanafi, A. Fleming, Z. Leong, and G. Macfarlane, "Effect of RANS-based turbulence models on nonlinear wave generation in a two-phase numerical wave tank," Prog. Comput. Fluid Dyn., vol. 17, no. 3, pp. 141-158, 2017.

[30] Z. Liu, B. S. Hyun, and K. Y. Hong, "Application of numerical wave tank to OWC air chamber for wave energy conversion," Proc. Int. Offshore Polar Eng. Conf., vol. 8, pp. 350-356, 2008.

[31] M. Zabihi, S. Mazaheri, and A. R. Mazyak, "Wave Generation in a Numerical Wave Tank," 17th Mar. Ind. Conf. 22-25 December2015 - Kish Isl., vol. 2017, no. 2, p. 11, 2015.

[32] A. Clément, "Coupling of two absorbing boundary conditions for 2D time-domain simulations of free surface gravity waves," J. Comput. Phys., vol. 126, no. 1, pp. 139-151, 1996.

[33] C. M. Dong and C. J. Huang, "On a 2-D numerical wave tank in viscous fluid," Proc. Int. Offshore Polar Eng. Conf., vol. 3, pp. 148-155, 2001.

[34] J. T. Batina, "Using Unstructured Dynamic Meshes," AIAA J., vol. 28, no. 8, pp. 1381-1388, 1990.

[35] J. F. Antaki, G. E. Blelloch, O. Ghattas, I. Malcevic, G. L. Miller, and N. J. Walkington, "a Parallel Dynamic-Mesh Lagrangian Method for Simulation of Flows With Dynamic Interfaces," vol. 00, no. c, pp. 26-26, 2015.

[36] M. Hasan, A. Kabir, and Y. M. Akib, "Dynamic stall investigation of two-dimensional vertical axis wind turbine blades using computational fluid dynamics," 8Th Bsme Int. Conf. Therm. Eng., vol. 2121, p. 120003, 2019.

[37] H. K. Esfeh, A. Azarafza, and M. K. A. Hamid, "On the computational fluid dynamics of PEM fuel cells (PEMFCs): An investigation on mesh independence analysis," RSC Adv., vol. 7, no. 52, pp. 32893-32902.

[38] S. B. Sarkar, Santanu, "I Nternational J Ournal of," Int. J. Energy Environ., vol. 4, no. 3, pp. 449-458, 2013.

[39] M. Anbarsooz, M. Passandideh-Fard, and M. Moghiman, "Fully nonlinear viscous wave generation in numerical wave tanks," Ocean Eng., vol. 59, pp. 73-85.

[40] C. Windt, J. Davidson, and J. V. Ringwood, "High-fidelity numerical modelling of ocean wave energy systems: A review of computational fluid dynamics-based numerical wave tanks," Renew. Sustain. Energy Rev., vol. 93, no. May, pp. 610-630, 2018.

[41] W. P. Jones and B. E. Launder, "The prediction of laminarization with a two-equation model of turbulence," Int. J. Heat Mass Transf., 1972.

[42] C. W. Hirt and B. D. Nichols, "Volume of fluid (VOF) method for the dynamics of free boundaries," J. Comput. Phys., vol. 39, no. 1, pp. 201-225, 1981.